nature physics

ARTICLES

https://doi.org/10.1038/s41567-017-0026-3

Wall roughness induces asymptotic ultimate turbulence

Xiaojue Zhu[1,5], Ruben A. Verschoof[1,5], Dennis Bakhuis[1], Sander G. Huisman[1], Roberto Verzicco[1,2], Chao Sun[1,3*] and Detlef Lohse[1,3,4*]

Turbulence governs the transport of heat, mass and momentum on multiple scales. In real-world applications, wall-bounded turbulence typically involves surfaces that are rough; however, characterizing and understanding the effects of wall roughness on turbulence remains a challenge. Here, by combining extensive experiments and numerical simulations, we examine the paradigmatic Taylor–Couette system, which describes the closed flow between two independently rotating coaxial cylinders. We show how wall roughness greatly enhances the overall transport properties and the corresponding scaling exponents associated with wall-bounded turbulence. We reveal that if only one of the walls is rough, the bulk velocity is slaved to the rough side, due to the much stronger coupling to that wall by the detaching flow structures. If both walls are rough, the viscosity dependence is eliminated, giving rise to asymptotic ultimate turbulence—the upper limit of transport—the existence of which was predicted more than 50 years ago. In this limit, the scaling laws can be extrapolated to arbitrarily large Reynolds numbers.

The vast majority of studies on wall-bounded turbulence assumes smooth walls, but in engineering applications, and even more so in nature, flow boundaries are in general rough, which leads to a coupling of the small roughness scale to the much larger outer length scale of the turbulent flow. This holds for the atmospheric boundary layer over forest canopies or buildings, for geophysical flows, in oceanography, but also for many industrial flows such as pipe flow, for which the presumably most famous (although controversial) study on roughness was performed[1]. For more recent works on the effect of wall roughness in (pipe or channel) turbulence we refer to various studies[2–5], reviews[6,7] or textbooks[8,9].

Rather than the open-channel or pipe flow, here we use a Taylor–Couette (TC) facility[10], which is a closed system that obeys global balances and at the same time allows for both accurate global and local measurements. The overall torque τ in TC flow that keeps the cylinders at constant angular velocity is connected with the spatially and time-averaged kinetic energy dissipation rate ϵ_u. This can be expressed in terms of the friction factor[8–10]

$$C_f = \frac{\tau}{\ell\rho_f\nu^2\left(\mathrm{Re_i}-\eta\mathrm{Re_o}\right)^2} = \frac{\pi\eta}{(1-\eta)}\frac{\epsilon_u}{\left(U_i-\eta U_o\right)^3/\left(r_i+r_o\right)} \quad (1)$$

Here $U_{i,o}$ are the velocities of the inner and outer cylinders, $r_{i,o}$ their radii, ν the kinematic viscosity (together defining the inner and outer Reynolds numbers $\mathrm{Re}_{i,o}=U_{i,o}d/\nu$), ρ_f the density of the fluid, ℓ the height of the TC cell, $d=r_o-r_i$ the gap width, and $\eta=r_i/r_o$ the ratio between the outer and inner cylinder radius. The key questions now are: how does C_f depend on the (driving) Reynolds number $\mathrm{Re}_{i,o}$ and how does wall roughness affect this relation?

Alternatively, the Re-dependence of C_f can be expressed as a 'Nusselt number' $\mathrm{Nu}_\omega=\tau/(2\pi\ell\rho_f J^\omega_{\mathrm{lam}})$ (that is, the dimensionless angular velocity flux normalized with the laminar flux[11] $J^\omega_{\mathrm{lam}}=2\nu r_i^2 r_o^2(\omega_i-\omega_o)/(r_o^2-r_i^2)$) depending on the Taylor number[10] $\mathrm{Ta}=[(1+\eta)^4/(64\eta^2)]d^2(r_i+r_o)^2(\omega_i-\omega_o)^2\nu^{-2}$, with $\omega_{i,o}$ the angular velocity of the inner and outer cylinders. This notation $\mathrm{Nu}_\omega(\mathrm{Ta})$ stresses the analogy between TC flow and Rayleigh–Bénard flow (RB)[12,13], the flow in a box heated from below and cooled from above, where Nu (the dimensionless heat flux) depends on the Rayleigh number Ra (the dimensionless temperature difference). For that system a study in 1962[14] postulated a so-called ultimate scaling regime[10,15–19]

$$\mathrm{Nu}\propto\mathrm{Ra}^{1/2}(\log\mathrm{Ra})^{-3/2} \quad (2)$$

for a fixed Prandtl number. In analogy, such an ultimate regime also exists for TC flow, namely

$$\mathrm{Nu}_\omega\propto\mathrm{Ta}^{1/2}(\log\mathrm{Ta})^{-3/2} \quad (3)$$

as worked out in a previous study[20]. In fact, in that study slightly different log dependences were derived, namely

$$\mathrm{Nu}\propto\mathrm{Ra}^{1/2}\mathcal{L}(\mathrm{Re}) \quad (4)$$

and

$$\mathrm{Nu}_\omega\propto\mathrm{Ta}^{1/2}\mathcal{L}(\mathrm{Re}) \quad (5)$$

where $\mathcal{L}(\mathrm{Re(Ra)})$ and $\mathcal{L}(\mathrm{Re(Ta)})$ are logarithmic dependences (see Methods and also ref. [20]). Irrespective of whether one takes the logarithmic dependences in equations (2), (3), (4) or (5), for smooth walls due to these log corrections the effective scaling exponent for the largest experimentally achievable Ra (Ta) values is only around 0.38 and not 1/2, that is, $\mathrm{Nu}\propto\mathrm{Ra}^{0.38}$ and $\mathrm{Nu}_\omega\propto\mathrm{Ta}^{0.38}$. This effective exponent of 0.38 has indeed been observed in large Ra RB

[1]Physics of Fluids Group and Max Planck Center Twente for Complex Fluid Dynamics, MESA+ Institute and J. M. Burgers Centre for Fluid Dynamics, University of Twente, Enschede, The Netherlands. [2]Dipartimento di Ingegneria Industriale, University of Rome Tor Vergata, Roma, Italy. [3]Center for Combustion Energy, Key Laboratory for Thermal Science and Power Engineering of Ministry of Education, Department of Energy and Power Engineering, Tsinghua University, Beijing, China. [4]Max Planck Institute for Dynamics and Self-Organization, Göttingen, Germany. [5]These authors contributed equally: Xiaojue Zhu and Ruben A. Verschoof. *e-mail: chaosun@tsinghua.edu.cn; d.lohse@utwente.nl

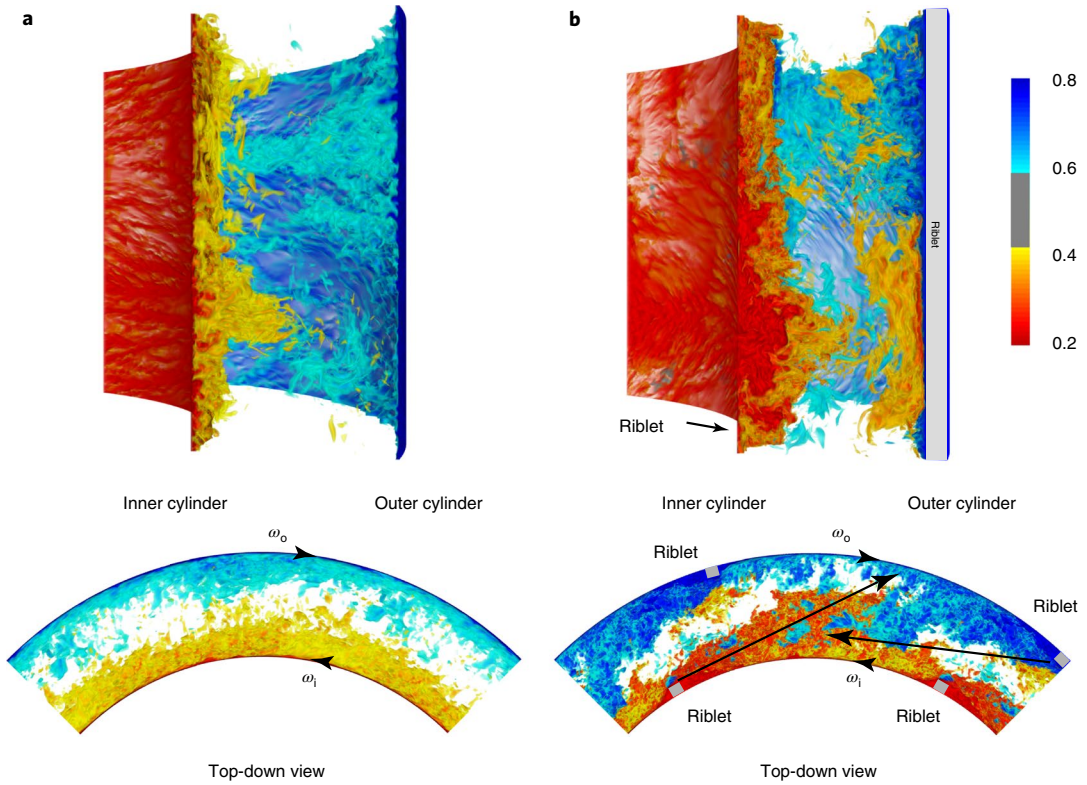

Fig. 1 | Plume structures for smooth and rough Taylor-Couette turbulence. In other words, turbulent flow between two co-axial rotating cylinders, where the inner cylinder rotates at angular velocity ω_i and outer cylinder at ω_o. Here the volume renderings of azimuthal velocity at $\mathrm{Ta}=2.15\times10^9$ and $\mathrm{Ro}^{-1}=-0.2$ are shown, from numerical simulations (see Methods for more details). **a**, Both cylinders are smooth. The plumes are generated on both cylinders and form the structure of Taylor rolls and they are concentrated in local regions and can not reach the other cylinder. **b**, Both cylinders are rough with 6 ribs of height $h=0.1d$. Even in the rough case, Taylor rolls still exist. Now the plumes are also generated on top of the roughness elements and shed to the opposing cylinder. The arrows in the top-down views illustrate the directions of plume shedding. All plots share the same colour coding, based on the value of the local azimuthal velocity.

experiments[16,17], large Ta TC experiments[10,18] and numerical simulations[10,19]. The log corrections, which are intimately connected with the logarithmic boundary layers[21] thus prevent the observation of the asymptotic ultimate regime exponent 1/2, which is the exponent of mathematically strict upper bounds for RB and TC turbulence[22–24]. Historically, whether such asymptotic 1/2 scaling exists or not has triggered enormous debate; see, for instance, ref.[12]. In the past two decades, great efforts have been put into reaching this regime with smooth boundaries, both experimentally and numerically. Today, this issue is often considered as one of the most important open problems in the thermal convection community. In fact, the exponent 1/2 has only been achieved with rough walls[25] as presumably a transient, local effective scaling, which saturates back to smaller exponent at even larger Ra[12,26,27], or in artificial configurations, such as numerical simulations of so-called homogeneous convective turbulence[28] with periodic boundary conditions and no boundary layers, or experimental realizations thereof[29,30].

The asymptotic exponent 1/2 in the Nu_ω versus Ta scaling law corresponds to C_f being independent of Re. Vice versa, expressed in terms of C_f, equations (3) and (5) can be written with a logarithmic dependence, analogous to the so-called Prandtl–von Kármán skin friction law[8,9,31] for pipe flow, that is

$$1/\sqrt{C_f} = a\,\log_{10}(\mathrm{Re}_i\sqrt{C_f}) + b \qquad (6)$$

which can be obtained by assuming that the boundary layer profiles at each cylinder wall are logarithmic and match at the middle gap[32–34]. Here a and b are fitting constants connected with the von Kármán constant κ.

How can the log correction be removed and thereby asymptotic ultimate turbulence with a 1/2 power law, or equivalently a Re-independent C_f for TC flow, be achieved? The path we will follow here is to introduce wall roughness[35–40]. By combining direct numerical simulations (DNS) and experiments (EXP), we explore five decades of Ta to present conclusive evidence that the 1/2 power law can be realized, thus achieving the asymptotic ultimate regime. Moreover, we will give a theoretical justification for the findings based on measurements of the global and local flow structures and extend the analysis to outer cylinder rotation.

Four cases will be considered: SS, SR, RS and RR, where the first (second) letter specifies the configuration of the inner (outer) cylinder, which can be either rough (R) or smooth (S). In both DNS and EXP, $\eta=0.716$. The cylinders were made rough by attaching 1 to 192 vertical ribs with identical heights ranging from 1.5% to 10% of d and a square cross-section over the entire TC cell on none, both or either one of the cylinders (see Methods). To give the reader an impression of the flow organization, typical flow structures of a smooth case and a rough case are shown in Fig. 1.

Global scaling relations

In this section we address the question of how roughness modifies the global scaling relations. First, we focus on the cases of 6 ribs with identical heights $h=0.075d$. The global dimensionless torques, $\mathrm{Nu}_\omega \propto \mathrm{Ta}^\gamma$, for the four cases, with increasing Ta and a fixed outer cylinder, are shown in Fig. 2a. Combining EXP and DNS, the range

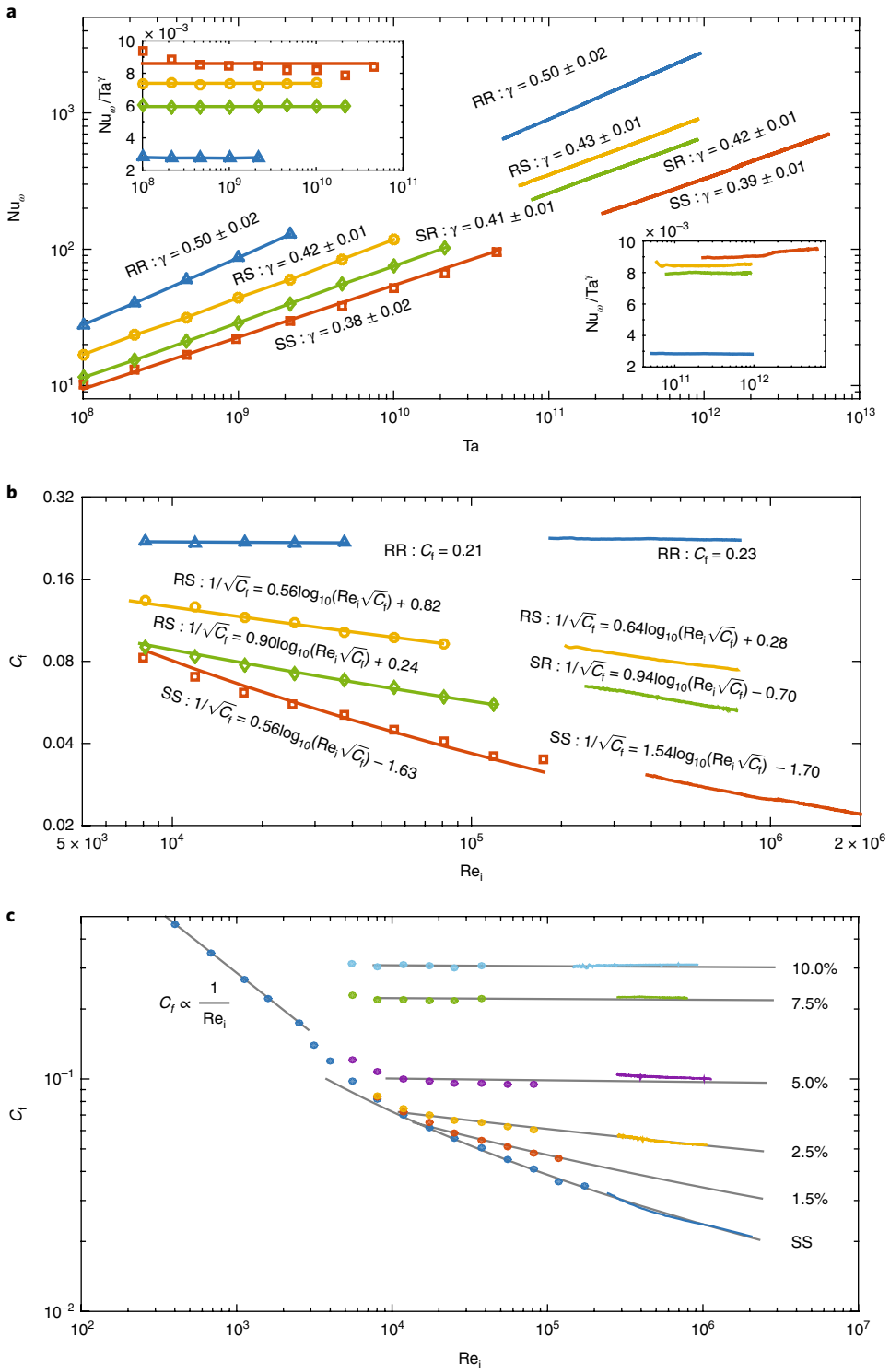

Fig. 2 | Global torque and friction factor scaling relations. DNS (left, symbols) and EXP (right, lines) are shown. **a**, The dimensionless torque Nu_ω as a function of the dimensionless angular velocity difference between the two cylinders Ta. Four cases are shown, with the exponent γ in the power law relation $Nu_\omega \propto Ta^\gamma$ shown for each. The insets depict the compensated plots Nu_ω/Ta^γ for DNS (left) and EXP (right), showing the quality of the scaling. **b**, Fricition factor C_f as a function of inner cylinder Reynolds number Re_i. The lines for the DNS show the best fits of the Prandtl friction law $1/\sqrt{C_f} = a\ \log_{10}(Re_i\sqrt{C_f}) + b$, with all prefactors shown in the figures. For **a**,**b**, 6 ribs were used and the roughness height is $h = 0.075d$. For the RR case, Re_i-independent friction factors are revealed. **c**, C_f for RR cases with 6 ribs of different heights, ranging from 1.5% to 10% of d. The SS case is shown for comparison. The grey lines are the best fits of the Prandtl friction law for each case in combination of experimental and numerical data.

of Taylor number studied here extends over five decades. Similar to what was shown in various recent studies[10,16,19,34,41,42] for the SS case, effective scalings of $Nu_\omega \propto Ta^{0.39\pm0.01}$ and $Nu_\omega \propto Ta^{0.38\pm0.02}$ are observed in the EXP and DNS, respectively. These findings both correspond to the ultimate regime with logarithmic corrections[14,20] and demonstrate the excellent agreement between DNS and EXP.

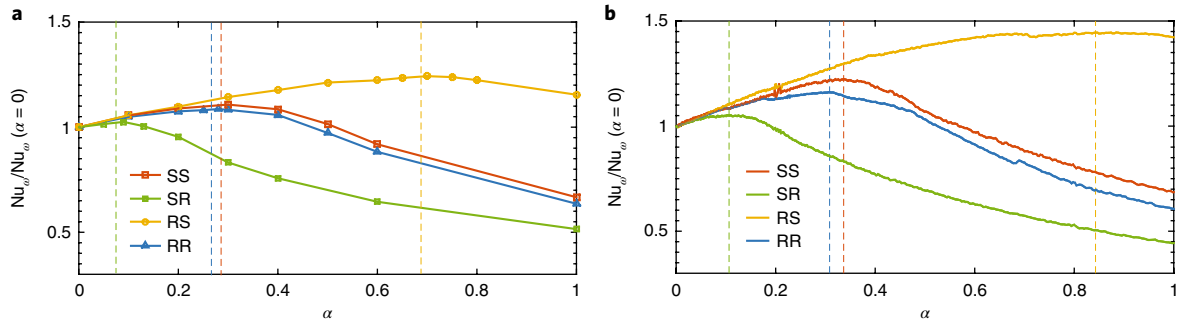

Fig. 3 | Optimal transport peaks for smooth and rough cases. Nu_ω as function of a for constant driving strength, normalized by its value for $a=0$. For both EXP and DNS, 6 ribs were used and the roughness height is $h=0.075d$. **a**, DNS with $Ta=1\times10^9$. The optimal transport peaks are located at $a^{DNS}_{opt,SS}=0.30\pm0.03$, $a^{DNS}_{opt,SR}=0.09\pm0.03$, $a^{DNS}_{opt,RS}=0.69\pm0.05$ and $a^{DNS}_{opt,RR}=0.28\pm0.03$. **b**, Experiments with $Ta=4\times10^{11}$. The optimal transport peaks for the four cases are located at $a^{EXP}_{opt,SS}=0.34$, $a^{EXP}_{opt,SR}=0.11$, $a^{EXP}_{opt,RS}=0.84$ and $a^{EXP}_{opt,RR}=0.31$. All optimal transport peaks are indicated by the colour-coded dashed lines.

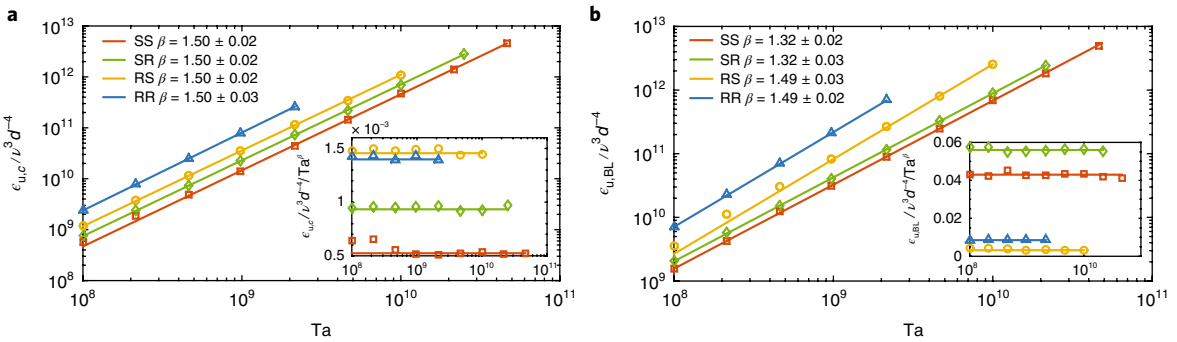

Fig. 4 | Local energy dissipation rate from simulations. Local energy dissipation rate in the bulk $\epsilon_{u,c}$ (at the centre of the gap, averaged over the height) and in the inner cylinder boundary layer $\epsilon_{u,BL}$ (averaged in the range from the wall to the distance corresponding to the maximum root mean square of the azimuthal velocity) as a function of Ta, with β as the scaling exponent. For the rough cases, 6 ribs were used and the roughness height is $h=0.1d$. The symbols are the numerical data and the lines show the best fits. **a**, The bulk energy dissipation rate follows $\epsilon_{u,c}\propto Ta^{1.50}\propto Re_i^3$, irrespective of whether the wall is smooth or rough. **b**, The boundary layer dissipation rate at the inner wall follows $\epsilon_{u,BL}\propto Ta^{1.32}$ for the cases with smooth walls, whereas it scales with $\epsilon_{u,BL}\propto Ta^{1.50}$ for the cases with a rough inner wall.

Dramatic enhancements of the torques are clearly observed with the introduction of wall roughness, resulting in the sharp increase of Nu_ω from $\mathcal{O}(10^2)$ to $\mathcal{O}(10^3)$. Specifically, when only a single cylinder is rough, the logarithmic corrections reduce and the scaling exponents marginally increase, implying that the scaling is dominated by the single smooth wall. For the RR case, the best power law fits give $Nu_\omega\propto Ta^{0.50\pm0.02}$, both for the numerical and experimental data, suggesting that the logarithmic corrections are thoroughly cancelled. This state with the scaling exponent 1/2 corresponds to the asymptotic ultimate turbulence predicted by earlier work[14]. The compensated plots of insets of Nu_ω/Ta^γ show the robustness and the quality of the scalings.

When expressing the relation between the global transport properties and the driving force in terms of the Re-dependence of C_f, we obtain Fig. 2b. Following the approach in ref. [32], for the SS case, the fitting parameters a and b here yield von Kármán constant $\kappa=0.44\pm0.01$, which is slightly larger than the standard value of 0.41 due to the curvature effect[21,33,43]. This agrees well with the previous measurements on TC with smooth walls[44]. For the RR case, for large enough driving C_f is found to be independent of Re_i, but dependent on roughness height, specifically, $C_f=0.21$ in the DNS and $C_f=0.23$ in the EXP for $h=0.075d$. The results here are consistent with the asymptotic ultimate regime scaling 1/2 for Nu_ω and indicate that the Prandtl–von Kármán log law of the wall[8,9] with wall roughness can be independent of Re_i[1,6–9], which has been verified recently for TC flow[45]. For the RS and SR cases, one boundary is rough and the other is smooth such that the friction law lies in between RR and SS lines.

We further show the RR case with ribs of different heights, ranging from 1.5% to 10% of d in Fig. 2c, displaying its similarity with the Nikuradse[1] and Moody[46] diagrams for pipe flow. It can be seen that once $h\geq0.05d$ and $Re_i\geq8.1\times10^3$ ($Ta\geq10^8$), the asymptotic ultimate regime can always be achieved in both DNS and EXP.

Analogously, we note that in pipe flow, the same phenomenon of Re-independent C_f with wall roughness was observed in the fully rough regime[1,6–9], where the characteristic heights of the roughness elements in wall units $h^+>70$[8,9]. In contrast, for $Ta=10^8$, for the roughness height $h/d=0.05$, $h/d=0.075$ and $h/d=0.10$, $h^+=51$, $h^+=61$ and $h^+=71$, respectively. Indeed, almost all of our data are in the fully rough regime for cases with $h\geq0.05d$ and $Ta\geq10^8$, thus corroborating the conclusion that adopting wall roughness is one way to achieve asymptotic ultimate turbulence in TC.

We now interpret the asymptotic ultimate torque scalings through an extension of the Grossmann–Lohse (GL) theory[20], by accounting for the Prandtl–von Kármán log law of the wall[9] in the presence of roughness. To demonstrate this extension, for simplicity we take as example the case of only inner cylinder rotation. For a smooth wall, the energy dissipation rate in the log region scales with $\epsilon_u d^4/\nu^3\propto Re_i^3(u_\tau/U_i)^3\ln(Re_i u_\tau/U_i)$[20], which stems from the integration of the Prandtl-von Kármán log law of the wall, where

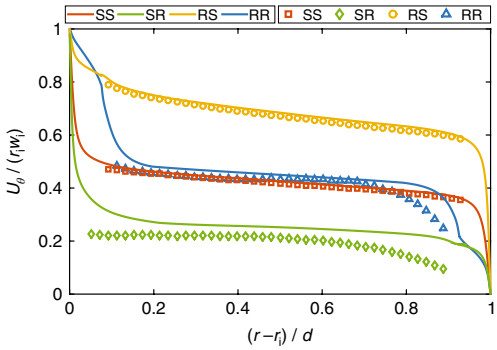

Fig. 5 | Mean velocity profiles. Normalized azimuthal velocity $U_\theta(r)/(r_i\omega_i)$ profiles as a function of the normalized radius $(r-r_i)/d$ for inner cylinder rotation only. For both EXP (symbols) and DNS (lines), 6 ribs were used and the roughness height is $h=0.075d$. Experimental and numerical data are shown in the same figure. $\mathrm{Re_i}=5\times10^5$ (EXP) and $\mathrm{Re_i}=3.74\times10^4$ (DNS). The experimental results were obtained using PIV.

u_τ is the friction velocity and U_i the velocity of the inner cylinder. The log term in the law is dependent on $\mathrm{Re_i}$, which is the origin of the logarithmic correction term $\mathcal{L}(\mathrm{Re}) = (u_\tau / U_i)^3 \ln(\mathrm{Re_i} u_\tau / U_i)$ and thus for the deviation from the asymptotic ultimate regime scaling $\epsilon_u d^4 / \nu^3 \propto \mathrm{Re_i^3}$, leading to a decrease in the effective scaling exponent. However, with roughness, as stated before, the log term in the law of the wall becomes independent of $\mathrm{Re_i}$[6–9,45], which correspondingly renders this correction constant. Translating this argument for the energy dissipation rate $\epsilon_u(\mathrm{Re_i})$ back to the dimensionless torque Nu_ω and the driving force Ta[11], we obtain $\mathrm{Nu}_\omega \propto \mathrm{Ta}^{1/2}$, that is, the effect of the logarithmic term on the scaling vanishes; see Methods for details.

One distinct difference between TC and pipe flow is that in a TC system the inner and outer cylinders can rotate independently, resulting in a second control parameter: the rotation ratio $a=-\omega_o/\omega_i$ of the two cylinders. Just as for smooth walls[10,41], for rough walls the $\mathrm{Nu}_\omega \propto \mathrm{Ta}^\gamma$ scaling exponents are independent of a in the studied rotation ratio regime; see Supplementary Fig. 2. As known since 1923[47], the inner cylinder rotation has a destabilizing effect on the flow, whereas outer cylinder rotation has a stabilizing effect. For TC flow with smooth walls, it was found that the optimal transport rotation ratio a_{opt} between the two cylinders, where the torque reaches the maximum for a specific driving Ta, is around $a_{\mathrm{opt}}=0.36$[48,49], and not zero, as one may have assumed. This is attributed to the existence of the strong Taylor rolls between the counter-rotating cylinders when $a \approx a_{\mathrm{opt}}$. Only for strong enough counter-rotation ($a > a_{\mathrm{opt}}$) does the stabilization through the counter-rotating outer cylinder take over[50]. Here, we address the question whether this optimal transport rotation ratio shifts or stays the same in the presence of roughness. The results are shown in Fig. 3. We find that when either one of the cylinders is rough, the effect of that rough cylinder is enhanced in several ways, as we will now elaborate.

In the SR case, $a^{\mathrm{DNS}}_{\mathrm{opt,SR}}=0.09\pm0.03$ and $a^{\mathrm{EXP}}_{\mathrm{opt,SR}}=0.11$, that is, little outer cylinder rotation is necessary to reduce the angular velocity transport with the help of the roughness elements on it, which are thus not so effective. In contrast, a rough inner cylinder is much more effective in enhancing the momentum transport. The optimal transport peak for the RS case occurs at much larger rotation ratio, $a^{\mathrm{DNS}}_{\mathrm{opt,RS}}=0.69\pm0.05$ and $a^{\mathrm{EXP}}_{\mathrm{opt,RS}}=0.84$, as very strong outer cylinder rotation is needed to suppress turbulence originating from the rough inner cylinder. In this case the stabilizing effect of the smooth outer cylinder becomes inefficient.

Finally, in the RR case, the effects of the inner cylinder and outer cylinder are balanced in a similar way to the SS case, resulting in similar values of $a^{\mathrm{DNS}}_{\mathrm{opt,RR}}=0.28\pm0.03$ and $a^{\mathrm{EXP}}_{\mathrm{opt,RR}}=0.31$ to those found in the SS case ($a^{\mathrm{DNS}}_{\mathrm{opt,SS}}=0.30\pm0.03$ and $a^{\mathrm{EXP}}_{\mathrm{opt,SS}}=0.34$). At optimal rotation ratio a_{opt}, the enhanced shear is caused by Taylor rolls[19,49,51,52]. This indicates that even in the presence of roughness, Taylor rolls still exist, as visible in Fig. 1b. We further notice that the optimal transport properties are dependent on the roughness height, as shown in Supplementary Fig. 3. As expected, when the roughness height is smaller, a_{opt} for the SR and RS cases are closer to a_{opt} for the SS case. On the contrary, when the roughness height is larger, a_{opt} for the SR and RS cases deviates more from a_{opt} for the SS case. This can be clearly seen from Supplementary Fig. 4.

Local flow organization and profiles

We have so far focused on the global transport properties. However, the details of the boundary layer–bulk interaction, and in particular how the local scalings of the energy dissipation rates affect the global ones, are still unknown. To verify theory outlined above, from our DNS data we split the mean energy dissipation rate (equation (1)) into boundary layer and bulk contributions, following the GL approach[53,54]. In Fig. 4a, the local energy dissipation rates at mid-gap $\epsilon_{u,c}$ are shown as a function of Ta (only inner cylinder rotation, $a=0$). It is clear that no matter whether the wall is smooth or rough, the bulk energy dissipation rate follows $\epsilon_{u,c} \propto \mathrm{Ta}^{3/2} \propto \mathrm{Re_i^3}$, which corresponds to the asymptotic ultimate regime without any logarithmic correction. In analogy, for RB turbulence, the same scaling exponent $\epsilon_{u,c} \propto \mathrm{Ra}^{3/2}$ was reported in earlier studies[55,56]. Therefore, the crucial element determining the overall scaling is the dissipation rate in the boundary layer. To further confirm this, in Fig. 4b we show the local energy dissipation rates of the boundary layer $\epsilon_{u,\mathrm{BL}}$ (averaged in the range from the wall to the distance corresponding to the maximum root mean square of the azimuthal velocity). For the case with smooth walls, we find $\epsilon_{u,\mathrm{BL}} \propto \mathrm{Ta}^{1.32}$ because of the $\mathrm{Re_i}$-dependent velocity profile, while for the boundary layers at rough walls we have $\epsilon_{u,\mathrm{BL}} \propto \mathrm{Ta}^{3/2}$ because, as shown above, roughness cancels out the $\mathrm{Re_i}$-dependence in $\mathcal{L}(\mathrm{Re_i})$ and thus restores the asymptotic ultimate regime scaling. The competition between the boundary layer and bulk ultimately determines the global scalings.

We now detail the origin of the enhanced torque. With roughness, the main contribution to the torque originates from the pressure differences between the side surfaces of rough elements, rather than from viscous forces[6–9,45]. With roughness, we therefore expect the shear rate close to the rough wall to decrease significantly compared with the smooth case. This is clearly shown in Fig. 5: with smooth cylinders, the normalized velocity profiles are characterized by a bulk region in which the velocity is relatively constant, $U_\theta=0.45 r_i\omega_i$ (whereas for pipe flow, this is not the case, see Supplementary Fig. 5). When one single cylinder is rough, the bulk velocity is completely dominated by the velocity of the rough cylinder, or in other words, the bulk is enslaved to the rough wall. In the RR case, as there the torque is dominated by pressure forces, the shear rate at the rough cylinder is still smaller than the smooth case. The implication is that with roughness, a larger fraction of energy dissipates in the bulk, and thus the system becomes bulk-dominant. As mentioned before, the bulk energy dissipation rate follows $\epsilon_{u,c} \propto \mathrm{Ta}^{3/2}$, which implies the asymptotic ultimate regime. The more the bulk dominates the energy dissipation rate, the better the asymptotic ultimate regime manifests itself. This is indeed verified by the flow structure in Fig. 1, where for the rough case, the plumes shedding from the roughness elements on one wall elongate towards the other wall and push more energetic fluid elements into the bulk, compared with the smooth case, leading to more energy dissipation in the bulk.

Controlling ultimate turbulence

To bridge the gap between the effective ultimate scaling exponent 0.38 for the smooth case[10,16,17,19] and the asymptotic ultimate scaling exponent 0.5 for the RR case and thus to actively control ultimate turbulence, we vary the sparseness of the roughness elements

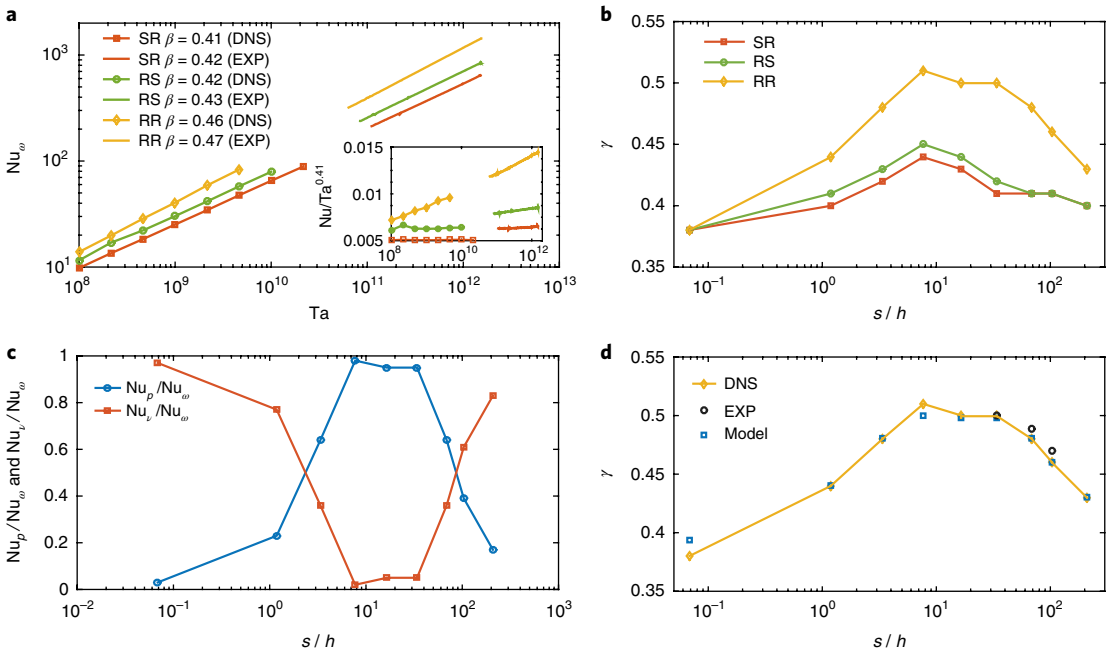

Fig. 6 | Dependence on the roughness sparseness. a, The dimensionless torque as a function Ta: DNS (left), and EXP (right) for the case of two ribs with height $h=0.075d$. For the RR case, the asymptotic ultimate regime is not yet achieved, in contrast to Fig. 2, when there are six ribs, for which the exponent is 0.5. The inset plot depicts the compensated scaling $Nu_\omega/Ta^{0.41}$ for DNS (left) and EXP (right), showing the quality of the exponent. **b**, Effective scaling exponent γ for varying spacing distance s/h between the ribs. The number of ribs varies from 1 to 196 and correspondingly, the spacing s/h varies from 208.44 to 0.07 at the inner cylinder. To get each value of γ, five simulations between $Ta=10^8$ and $Ta=10^9$ were performed. **c**, Contributions Nu_p (from pressure drag) and Nu_ν (from viscous drag) to the global Nu_ω at $Ta=4.6\times10^8$ with varying the spacing s/h between the ribs. The data are collected from DNS. The separation into the two parts is performed at the inner cylinder for the RR case. Clearly, when the pressure forces are dominant, γ is closer to 1/2 and when viscous forces are dominant, γ is closer to 0.38 (Fig. 6b). **d**, Comparison of γ between the DNS results (RR case), EXP results (RR case) and the model results (based on equation (7)) with varying spacing s/h between the ribs.

while keeping the height of the riblets fixed at 7.5% of the gap width. To show how this will change the results, as an example we show the Nu_ω versus Ta scaling for the case of 2 ribs (very sparse) in Fig. 6a. The effective scaling exponent γ for the RR case is then smaller than 0.5 (that is, 0.47), so the asymptotic ultimate regime is not yet achieved in this situation, in contrast to Fig. 2, when there are six ribs, for which $\gamma=0.5$. We then continuously vary the number of ribs from 1 (very sparse) to 192 (very dense). Correspondingly, the spacing between the rough elements s/h mounted on the inner wall varies from 208.44 to 0.07. We note that in pipe and BL flows, there is a distinction between k- and d-type roughness, and a close spacing will make the roughness behave more like d-type roughness than k-type roughness[6,7]. In Fig. 6b, we see that the effective scaling exponent is continuously changing with s/h. There is an optimal $s/h=7$ where the effective scaling exponent is the largest, corresponding to k-type roughness. To explain why the effective scaling exponent depends on s/h, in Fig. 6c we split the global Nu_ω into two parts, namely the viscous force contribution (Nu_ν) and the pressure force contribution (Nu_p). Clearly, when the effective scaling exponent is higher, the pressure forces are more dominant.

We propose a simple model that can recover the effective scaling exponent. The model is based on the fact that in the smooth case, only viscous forces contribute to Nu_ω, resulting in $Nu_\omega \propto Ta^{0.38}$. In contrast, when the pressure forces take over, we have $Nu_\omega \propto Ta^{0.5}$. Therefore, in the spirit of GL theory of RB[53], we combine these contributions to set

$$Nu_\omega = a\ Ta^{0.38} + b\ Ta^{0.5} \approx c\ Ta^{\gamma_m}, \qquad (7)$$

where $a=Nu_\nu/Ta^{0.38}$ and $b=Nu_p/Ta^{0.5}$ are the prefactors of the separated scalings for Nu_ν and Nu_p, respectively, which are roughness height dependent, and γ_m is the effective local exponent predicted by the model. Here for the $h=0.075d$ case we use the separation shown in Fig. 6c at $Ta=4.6\times10^8$ to determine a and b, and hence the effective exponent γ_m (other values of Ta can also be used and the results are similar). It can be seen that the model gives very good agreement with the DNS and EXP values (Fig. 6d). Clearly, different numbers of roughness elements can tune the scaling exponents and optimal transport properties, thus paving the way to control ultimate turbulence. The insight gained from this study provides valuable guidance not only for shear flows, but also for thermally driven turbulence with wall roughness in the ultimate regime, which is useful for a wide range of applications in industrial, geophysical, meteorological and oceanographical flows.

Methods

Methods, including statements of data availability and any associated accession codes and references, are available at https://doi.org/10.1038/s41567-017-0026-3.

Received: 28 April 2017; Accepted: 29 November 2017;
Published online: 12 February 2018

References

1. Nikuradse, J. Strömungsgesetze in rauhen Rohren. *Forschung. Arb. Ing. Wes.* **361**, (1933).
2. Hultmark, M., Vallikivi, M., Bailey, S. C. C. & Smits, A. J. Logarithmic scaling of turbulence in smooth-and rough-wall pipe flow. *J. Fluid. Mech.* **728**, 376–395 (2013).
3. Chan, L., MacDonald, M., Chung, D., Hutchins, N. & Ooi, A. A systematic investigation of roughness height and wavelength in turbulent pipe flow in the transitionally rough regime. *J. Fluid. Mech.* **771**, 743–777 (2015).

4. Chung, D., Chan, L., MacDonald, M., Hutchins, N. & Ooi, A. A fast direct numerical simulation method for characterising hydraulic roughness. *J. Fluid. Mech.* **773**, 418–431 (2015).
5. Squire, D. T. et al. Comparison of turbulent boundary layers over smooth and rough surfaces up to high Reynolds numbers. *J. Fluid. Mech.* **795**, 210–240 (2016).
6. Jiménez, J. Turbulent flows of rough walls. *Ann. Rev. Fluid Mech.* **36**, 173–196 (2004).
7. Flack, K. A. & Schultz, M. P. Roughness effects on wall-bounded turbulent flows. *Phys. Fluids* **26**, 101305 (2014).
8. Pope, S. B. *Turbulent Flow*. (Cambridge Univ. Press, Cambridge, 2000).
9. Schlichting, H. & Gersten, K. *Boundary Layer Theory* 8th edn (Springer, Berlin, 2000).
10. Grossmann, S., Lohse, D. & Sun, C. High Reynolds number Taylor-Couette turbulence. *Ann. Rev. Fluid Mech.* **48**, 53–80 (2016).
11. Eckhardt, B., Grossmann, S. & Lohse, D. Torque scaling in turbulent Taylor-Couette flow between independently rotating cylinders. *J. Fluid. Mech.* **581**, 221–250 (2007).
12. Ahlers, G., Grossmann, S. & Lohse, D. Heat transfer and large scale dynamics in turbulent Rayleigh-Bénard convection. *Rev. Mod. Phys.* **81**, 503 (2009).
13. Lohse, D. & Xia, K.-Q. Small-scale properties of turbulent Rayleigh-Bénard convection. *Ann. Rev. Fluid Mech.* **42**, 335–364 (2010).
14. Kraichnan, R. H. Turbulent thermal convection at arbitrary Prandtl number. *Phys. Fluids* **5**, 1374–1389 (1962).
15. Chavanne, X. et al. Observation of the ultimate regime in Rayleigh-Bénard convection. *Phys. Rev. Lett.* **79**, 3648–3651 (1997).
16. He, X., Funfschilling, D., Nobach, H., Bodenschatz, E. & Ahlers, G. Transition to the ultimate state of turbulent Rayleigh-Bénard convection. *Phys. Rev. Lett.* **108**, 024502 (2012).
17. He, X., Funfschilling, D., Bodenschatz, E. & Ahlers, G. Heat transport by turbulent Rayleigh-Bénard convection for $Pr = 0.8$ and $4 \times 10^{11} < Ra < 2 \times 10^{14}$: ultimate-state transition for aspect ratio $\Gamma = 1.00$. *New. J. Phys.* **14**, 063030 (2012).
18. Huisman, S. G., van Gils, D. P. M., Grossmann, S., Sun, C. & Lohse, D. Ultimate turbulent Taylor-Couette flow. *Phys. Rev. Lett.* **108**, 024501 (2012).
19. Ostilla-Mónico, R., van der Poel, E. P., Verzicco, R., Grossmann, S. & Lohse, D. Exploring the phase diagram of fully turbulent Taylor-Couette flow. *J. Fluid. Mech.* **761**, 1–26 (2014).
20. Grossmann, S. & Lohse, D. Multiple scaling in the ultimate regime of thermal convection. *Phys. Fluids* **23**, 045108 (2011).
21. Ostilla-Mónico, R., Verzicco, R., Grossmann, S. & Lohse, D. The near-wall region of highly turbulent Taylor-Couette flow. *J. Fluid. Mech.* **788**, 95–117 (2016).
22. Doering, C. & Constantin, P. Variational bounds on energy dissipation in incompressible flows: III. Convection. *Phys. Rev. E* **53**, 5957–5981 (1996).
23. Nicodemus, R., Grossmann, S. & Holthaus, M. Variational bound on energy dissipation in turbulent shear flow. *Phys. Rev. Lett.* **79**, 4170 (1997).
24. Plasting, S. C. & Kerswell, R. R. Improved upper bound on the energy dissipation rate in plane Couette flow: the full solution to Busse's problem and the Constantin-Doering-Hopf problem with one-dimensional background field. *J. Fluid. Mech.* **477**, 363–379 (2003).
25. Toppaladoddi, S., Succi, S. & Wettlaufer, J. S. Roughness as a route to the ultimate regime of thermal convection. *Phys. Rev. Lett.* **118**, 074503 (2017).
26. Xie, Y.-C. & Xia, K.-Q. Turbulent thermal convection over rough plates with varying roughness geometries. *J. Fluid. Mech.* **825**, 573–599 (2017).
27. Zhu, X., Stevens, R. A. J. M., Verzicco, R. & Lohse, D. Roughness-facilitated local 1/2 scaling does not imply the onset of the ultimate regime of thermal convection. *Phys. Rev. Lett.* **119**, 154501 (2017).
28. Lohse, D. & Toschi, F. The ultimate state of thermal convection. *Phys. Rev. Lett.* **90**, 034502 (2003).
29. Gibert, M., Pabiou, H., Chilla, F. & Castaing, B. High-Rayleigh-number convection in a vertical channel. *Phys. Rev. Lett.* **96**, 084501 (2006).
30. Cholemari, M. & Arakeri, J. Axially homogeneous, zero mean flow buoyancy-driven turbulence in a vertical pipe. *J. Fluid. Mech.* **621**, 69–102 (2009).
31. von Kármán, T. Über laminare und turbulente Reibung. *Z. Angew. Math. Mech.* **1**, 233–252 (1921).
32. Lathrop, D. P., Fineberg, J. & Swinney, H. S. Turbulent flow between concentric rotating cylinders at large Reynolds numbers. *Phys. Rev. Lett.* **68**, 1515–1518 (1992).
33. Huisman, S. G. et al. Logarithmic boundary layers in strong Taylor-Couette turbulence. *Phys. Rev. Lett.* **110**, 264501 (2013).
34. Ostilla-Mónico, R., van der Poel, E. P., Verzicco, R., Grossmann, S. & Lohse, D. Boundary layer dynamics at the transition between the classical and the ultimate regime of Taylor-Couette flow. *Phys. Fluids* **26**, 015114 (2014).
35. Shen, Y., Tong, P. & Xia, K.-Q. Turbulent convection over rough surfaces. *Phys. Rev. Lett.* **76**, 908–911 (1996).
36. Du, Y. B. & Tong, P. Turbulent thermal convection in a cell with ordered rough boundaries. *J. Fluid. Mech.* **407**, 57–84 (2000).
37. Roche, P. E., Castaing, B., Chabaud, B. & Hebral, B. Observation of the 1/2 power law in Rayleigh-Bénard convection. *Phys. Rev. E* **63**, 045303 (2001).
38. van den Berg, T. H., Doering, C., Lohse, D. & Lathrop, D. Smooth and rough boundaries in turbulent Taylor-Couette flow. *Phys. Rev. E* **68**, 036307 (2003).
39. Tisserand, J. C. et al. Comparison between rough and smooth plates within the same Rayleigh-Bénard cell. Phys. *Fluids* **23**, 015105 (2011).
40. Wei, P., Chan, T.-S., Ni, R., Zhao, X.-Z. & Xia, K.-Q. Heat transport properties of plates with smooth and rough surfaces in turbulent thermal convection. *J. Fluid. Mech.* **740**, 28–46 (2014).
41. van Gils, D. P. M., Huisman, S. G., Bruggert, G. W., Sun, C. & Lohse, D. Torque scaling in turbulent Taylor-Couette flow with co- and counter-rotating cylinders. *Phys. Rev. Lett.* **106**, 024502 (2011).
42. Brauckmann, H. J. & Eckhardt, B. Direct numerical simulations of local and global torque in Taylor-Couette flow up to $Re = 30\,000$. *J. Fluid. Mech.* **718**, 398–427 (2013).
43. Grossmann, S., Lohse, D. & Sun, C. Velocity profiles in strongly turbulent Taylor-Couette flow. *Phys. Fluids* **26**, 025114 (2014).
44. Lewis, G. S. & Swinney, H. L. Velocity structure functions, scaling, and transitions in high-Reynolds-number Couette-Taylor flow. *Phys. Rev. E* **59**, 5457–5467 (1999).
45. Zhu, X., Verzicco, R. & Lohse, D. Disentangling the origins of torque enhancement through wall roughness in Taylor-Couette turbulence. *J. Fluid. Mech.* **812**, 279–293 (2017).
46. Moody, L. F. Friction factors for pipe flow. *Trans. ASME* **66**, 671–684 (1944).
47. Taylor, G. I. Stability of a viscous liquid contained between two rotating cylinders. *Phil. Trans. R. Soc. A* **223**, 289–343 (1923).
48. Brauckmann, H. J. & Eckhardt, B. Intermittent boundary layers and torque maxima in Taylor-Couette flow. *Phys. Rev. E* **87**, 033004 (2013).
49. Huisman, S. G., van der Veen, R. C. A., Sun, C. & Lohse, D. Multiple states in highly turbulent Taylor-Couette flow. *Nat. Commun.* **5**, 3820 (2014).
50. van Gils, D. P. M., Huisman, S. G., Grossmann, S., Sun, C. & Lohse, D. Optimal Taylor-Couette turbulence. *J. Fluid. Mech.* **706**, 118–149 (2012).
51. Chouippe, A., Climent, E., Legendre, D. & Gabillet, C. Numerical simulation of bubble dispersion in turbulent Taylor-Couette flow. *Phys. Fluids* **26**, 043304 (2014).
52. Martínez-Arias, B., Peixinho, J., Crumeyrolle, O. & Mutabazi, I. Effect of the number of vortices on the torque scaling in Taylor-Couette flow. *J. Fluid. Mech.* **748**, 756–767 (2014).
53. Grossmann, S. & Lohse, D. Scaling in thermal convection: a unifying view. *J. Fluid. Mech.* **407**, 27–56 (2000).
54. Grossmann, S. & Lohse, D. Thermal convection for large Prandtl number. *Phys. Rev. Lett.* **86**, 3316–3319 (2001).
55. Shang, X. D., Tong, P. & Xia, K.-Q. Scaling of the local convective heat flux in turbulent Rayleigh-Bénard convection. *Phys. Rev. Lett.* **100**, 244503 (2008).
56. Ni, R., Huang, S.-D. & Xia, K.-Q. Local energy dissipation rate balances local heat flux in the center of turbulent thermal convection. *Phys. Rev. Lett.* **107**, 174503 (2011).

Acknowledgements

We gratefully acknowledge V. Mathai for insightful discussions. We thank G. W. Bruggert and M. Bos, as well as G. Mentink and R. Nauta, for their technical support and D.P.M. van Gils and R. Ezeta for various discussions and help with the experiments. The work is financially supported by NWO-I, NWO-TTW, the Netherlands Center for Multiscale Catalytic Energy Conversion (MCEC), and a VIDI grant (No. 13477), all sponsored by the Netherlands Organisation for Scientific Research (NWO). C.S. acknowledges the financial support from Natural Science Foundation of China under Grant No. 11672156. Part of the simulations were carried out on the Dutch national e-infrastructure with the support of SURF Cooperative. We also acknowledge PRACE for awarding us access to Marconi at CINECA, Italy under PRACE project number 2016143351 and DECI resource ARCHER UK National Supercomputing Service with the support from PRACE under project 13DECI0246.

Author contributions

X.Z., S.G.H., R.A.V., R.V., C.S. and D.L. conceived the ideas. X.Z. performed the numerical simulations. R.A.V. and D.B. performed the measurements. X.Z. and R.A.V. analysed the data. X.Z., R.A.V. and D.L. wrote the paper. R.V., C.S. and D.L. supervised the project. All authors discussed the physics and proofread the paper.

Competing interests

The authors declare no competing financial interests.

Additional information

Supplementary information is available for this paper at https://doi.org/10.1038/s41567-017-0026-3.

Reprints and permissions information is available at www.nature.com/reprints.

Correspondence and requests for materials should be addressed to C.S. or D.L.

Publisher's note: Springer Nature remains neutral with regard to jurisdictional claims in published maps and institutional affiliations.

Methods

Experimental methods. *Experimental apparatus.* The experiments were performed in the Twente Turbulent Taylor-Couette facility (T^3C)[57], consisting of two independently rotating concentric cylinders. The setup has an inner cylinder with a radius of $r_i = 200$ mm and an outer cylinder with a radius of $r_o = 279.4$ mm, resulting in a radius ratio of $\eta = r_i/r_o = 0.716$ and a gap width of $d = r_o - r_i = 79.4$ mm. The gap is filled with water with a temperature of $T \approx 20$ °C. In this work, the inner and outer cylinder rotate up to $\omega_i/(2\pi) = 7.5$ Hz and $\omega_o/(2\pi) = 5$ Hz, respectively, resulting in Reynolds numbers up to $\mathrm{Re_i} = \omega_i r_i d/\nu = 7.5\times10^5$ and $\mathrm{Re_o} = \omega_o r_o d/\nu = 7\times10^5$. The cylinders have a height of $L = 927$ mm, resulting in an aspect ratio of $\Gamma = L/(r_o - r_i) = 11.7$. The end plates rotate with the outer cylinder. The cylinders were made rough by attaching 2, 3 or 6 vertical strips with a square cross-section (four roughness heights: 2×2 mm (2.5% of the gap width), 4×4 mm (5% of the gap width), 6×6 mm (7.5% of the gap width) and 8×8 mm (10% of the gap width)) over the entire height on none, both or either one of the cylinders.

Torque measurements. The torque is measured with a co-axial torque transducer (Honeywell 2404–5 K, maximum capacity of 565 Nm), located inside the inner cylinder, to avoid measurement errors due to seals and bearing friction, as shown in Supplementary Fig. 1. For the SS case, the inner cylinder consisted of 3 different compartments, in which torque was measured in the middle section to exclude end plate effects. For the rough cases, we measure torque over the entire height of the cylinder.

Velocity measurements. Planar particle image velocimetry (PIV) measurements were performed in the $\theta - r$ plane at mid-height ($z = L/2$). We used a high-resolution sCMOS camera (pco.edge camera with 2,560 pixel × 2,160 pixel resolution), which was operated in double frame mode, as depicted in Supplementary Fig. 1. We recorded images through transparent windows in the bottom plate. The flow was illuminated from the side with a pulsed laser (532 nm Quantel Evergreen 145 Nd:YLF). The water was seeded with 20 µm fluorescent polymer particles (PMMA-RhB-10 by Dantec). The sheet thickness was approximately 1 mm. The PIV measurements were processed using an iterative multi-pass method with final interrogation windows of 32 pixel × 32 pixel with 50% overlap and averaged over 500 image pairs per measurement. This results in the averaged azimuthal velocity profile $\langle u_\theta(r)\rangle$.

Numerical methods. The motion of the fluid is governed by the incompressible Navier–Stokes equations in the frame co-rotating with the outer cylinder

$$\frac{\partial \mathbf{u}}{\partial t} + \mathbf{u}\cdot\nabla\mathbf{u} = -\nabla p + \frac{f(\eta)}{\mathrm{Ta}^{1/2}}\nabla^2\mathbf{u} - \mathrm{Ro}^{-1}\mathbf{e}_z\times\mathbf{u} \tag{8}$$

$$\nabla\cdot\mathbf{u} = 0 \tag{9}$$

where $\mathbf{u}$ and p are the fluid velocity and pressure, respectively. $f(\eta)$ is a geometrical factor which has the form

$$f(\eta) = \frac{(1+\eta)^3}{8\eta^2} \tag{10}$$

Ta is the Taylor number and Ro the Rossby number, which characterizes the strength of the driving force. The rotation ratio $a = -\omega_o/\omega_i$ can alternatively be expressed as

$$\mathrm{Ro}^{-1} = \frac{2\omega_o d}{|\omega_i - \omega_o|\, r_i} = -2\frac{1-\eta}{\eta}\frac{a}{|1+a|} \tag{11}$$

The inner cylinder Reynolds number $\mathrm{Re_i} = r_i\omega_i d/\nu$ and outer cylinder Reynolds number $\mathrm{Re_o} = r_o\omega_o d/\nu$ are associated with Ta and Ro through

$$\mathrm{Re_i} = \frac{\mathrm{Ta}^{1/2}}{f(\eta)}\left(1 + \frac{\eta\ \mathrm{Ro}^{-1}}{2(1-\eta)}\right) \tag{12}$$

and

$$\mathrm{Re_o} = \frac{\mathrm{Ro}^{-1}\mathrm{Ta}^{1/2}}{2f(\eta)(1-\eta)} \tag{13}$$

The governing equations are solved using an energy conserving second-order finite-difference code[58], in combination with an immersed-boundary method[59,60] to deal with the roughness. To achieve high-performance computation, a two-dimensional MPI decomposition technique (MPI-pencil)[61] is adopted. Weak and strong scaling tests show the linear behaviour of the code up to 64 K cores. The axial direction is periodic and thus the end plate effects[62] are eliminated. The radius ratio is chosen as $\eta = 0.716$. The aspect ratio of the computational domain $\Gamma = L/d$, where L is the axial periodicity length, is taken as $\Gamma = 2.09$. The ribs are distributed equidistantly in the azimuthal direction, in a similar way to the experimental implementation (with one more roughness height at 1.5% of the gap width). The computation box is tested to be large enough to capture the sign changes of the azimuthal velocity autocorrelation at the mid-gap, as suggested as a criterion for the box size[63]. An appropriate number of grid points is chosen to make sure that enough resolution has been employed, for example, at $\mathrm{Ta} = 2.15\times10^9$ for the RR case with 6 ribs at roughness height 10% of the gap width, 3,072×1,536×1,536 grid points are used.

Extention of the GL theory to the case with wall roughness. To explain the asymptotic ultimate scaling 1/2 found in this study, we first recall the origin of the logarithmic correction. We take the only inner rotation case as an example. We look at the local dissipation rate in the turbulent boundary layer[64], which can be approximated by

$$\epsilon_u(y) \approx u_\tau^3/(\kappa y) \tag{14}$$

where $u_\tau = \sqrt{\tau/(2\rho\pi r^2 L)}$ is the friction velocity. The radius r can be either the inner cylinder radius r_i or the outer one r_o, and y the distance from the wall. u_τ is connected with the inner cylinder velocity $U_i = r_i\omega_i$ through the law of the wall, which is shown to obey

$$\frac{u_\tau}{U_i} = \frac{\kappa}{\ln(B\ \mathrm{Re_i}u_\tau/U_i)} \tag{15}$$

For $\mathrm{Re_i}$ the pure inner cylinder rotation can be related to Ta through the expression $\mathrm{Ta} = [(1+\eta)^6/(64\eta^4)]\mathrm{Re_i^2}$, and B is a constant depending on the system geometry. By averaging the local dissipation rate along the radius, we can estimate the mean dissipation rate as

$$\begin{aligned}\epsilon_u &\propto \frac{2}{d}\int_0^{d/2}\epsilon_u(y)\mathrm{d}y \\ &= \nu^3 d^{-4}\ \mathrm{Re_i^3}\mathcal{L}(\mathrm{Re_i}) \\ &= \nu^3 d^{-4}\mathrm{Re_i^3}\left(\frac{u_\tau}{U_i}\right)^3\frac{2}{\kappa}\ln\left(\mathrm{Re_i}\frac{u_\tau}{U_i}\frac{1}{2}\right)\end{aligned} \tag{16}$$

Here we assume that logarithmic boundary layer extends from the wall to the mid-gap. Usually how far the log-layer extends depends on $\mathrm{Re_i}$ and can be a small fraction of the gap width, but still for both TC and pipe flows, taking the half gap width or radius is a reasonable approximation to derive the friction laws. The term $\mathcal{L}(\mathrm{Re_i}) = (u_\tau/U_i)^3\ln(\mathrm{Re_i}u_\tau/U_i)$, depending on $\mathrm{Re_i}$, is the logarithmic correction. Using the well-known exact relation between ϵ_u and Nu_ω,

$$\epsilon_u = \nu^3 d^{-4}\ \mathrm{Ta}(\mathrm{Nu}_\omega - 1)\left(\frac{\sqrt{\eta}}{(1+\eta)/2}\right)^8 \tag{17}$$

and with $\mathrm{Ta} \propto \mathrm{Re_i^2}$, one obtains

$$\frac{\epsilon_u}{\nu^3 d^{-4}} \propto \mathrm{Re_i^3}\mathcal{L}(\mathrm{Re_i}) \text{ and } \mathrm{Nu}_\omega \propto \mathrm{Ta}^{1/2}\,\mathcal{L}(\mathrm{Re_i}) \tag{18}$$

with the logarithmic correction $\mathcal{L}(\mathrm{Re_i})$ for both dissipation rate and torque scalings. It leads to a less steep increase of ϵ_u with increasing $\mathrm{Re_i}$ than in the Kolmogorov bulk, which scales as $\mathrm{Re_i^3}$, and hence decreases the torque scaling between Nu_ω and Ta from the asymptotic ultimate scaling 1/2 to the effective scaling 0.38, as mentioned before.

With both walls roughened, the log law in the fully rough regime ($u_\tau h/\nu > 70$; most of the rough cases in this study are in this regime) becomes

$$\frac{u_\tau}{U_i} = \frac{\kappa}{\ln(Bd/h)} \tag{19}$$

The momentum transfer between the wall and the fluid is accomplished by the shear, which in the fully rough regime occurs predominantly by the pressure forces on the side surfaces of the rough elements, rather than by viscous forces. In the ultimate regime ν is an irrelevant parameter, as reflected in the velocity profile (equation (19)) being independent of $\mathrm{Re_i}$. Replacing the velocity profile from the smooth one to the rough one in equations (14), (15) and (16), we find that the logarithmic correction term for ϵ_u turns into a constant and thus its effect on the scaling exponent vanishes. The mean dissipation rate and torque thus now scale as

$$\frac{\epsilon_u}{\nu^3 d^{-4}} \propto \mathrm{Re_i^3} \text{ and } \mathrm{Nu}_\omega \propto \mathrm{Ta}^{1/2} \tag{20}$$

which explains the asymptotic ultimate regime scaling seen in Fig. 2 for the RR case. In the RS or SR cases, the boundary layer at the smooth wall depends on $\mathrm{Re_i}$

while the boundary layer at the rough wall is independent of it. Therefore, in these cases the logarithmic correction is reduced but not totally cancelled.

Data availability. The data that support the plots within this paper and other findings of this study are available from the corresponding author upon reasonable request.

References

57. van Gils, D. P. M., Bruggert, G. W., Lathrop, D. P., Sun, C. & Lohse, D. The Twente turbulent Taylor-Couette (T3C) facility: strongly turbulent (multi-phase) flow between independently rotating cylinders. *Rev. Sci. Instr.* **82**, 025105 (2011).
58. Verzicco, R. & Orlandi, P. A finite-difference scheme for three-dimensional incompressible flow in cylindrical coordinates. *J. Comput. Phys.* **123**, 402–413 (1996).
59. Fadlun, E. A., Verzicco, R., Orlandi, P. & Mohd-Yusof, J. Combined immersed-boundary finite-difference methods for three-dimensional complex flow simulations. *J. Comput. Phys.* **161**, 35–60 (2000).
60. Yang, J. & Balaras, E. An embedded-boundary formulation for large-eddy simulation of turbulent flows interacting with moving boundaries. *J. Comput. Phys.* **215**, 12–40 (2006).
61. van der Poel, E. P., Ostilla-Mónico, R., Donners, J. & Verzicco, R. A pencil distributed finite difference code for strongly turbulent wall-bounded flows.*Comput. Fluids* **116**, 10–16 (2015).
62. Avila, M. Stability and angular-momentum transport of fluid flows between co-rotating cylinders. *Phys. Rev. Lett.* **108**, 124501 (2012).
63. Ostilla-Mónico, R., Verzicco, R. & Lohse, D. Effects of the computational domain size on direct numerical simulations of Taylor-Couette turbulence with stationary outer cylinder. *Phys. Fluids* **27**, 025110 (2015).
64. Landau, L. D. & Lifshitz, E. M. *Fluid Mechanics* (Pergamon, Oxford, 1987).